Research on Internal Model Control of Induction Motors Based on Luenberger Disturbance Observer

Zhonggang Yin, *Member, IEEE*, Cong Bai, Na Du, Chao Du, and Jing Liu

***Abstract*—Internal model control (IMC) has been used widely for its less computational burden, and simple implementation. By IMC, the disturbance including model mismatch, parameter variations, and other unstructured dynamic uncertainties cannot be eliminated effectively in the induction motor (IM) control system. To optimize the current-control performance of IM drives, a nonlinear current-control algorithm for the IM systems using IMC strategy based on a Luenberger disturbance observer (IMC-LDO) is proposed in this article. The time-varying disturbance has been considered in the IM system. Based on this system, the proposed method is derived, where a LDO is introduced to estimate the disturbance. To tune the proposed scheme properly, a stability analysis based on Jury criterion has been used to determine the selection of the observer gain. Comparative experimental results indicate that the proposed method improves the dynamic property and the robustness in case of parameter variations and step load change. The feasibility and effectiveness of the proposed method are verified by the experimental results.**

***Index Terms*—Induction motor (IM), internal model control (IMC), Luenberger disturbance observer (LDO), robustness.**

NOMENCLATURE

d, q	Rotary reference frame axes.
α, β	Stationary reference frame axes.
a, b, c	Three-phase reference frame axes.
$i_{s\alpha}$, $i_{s\beta}$	α-axis and β-axis stator currents, A.
i_{sd}, i_{sq}	d-axis and q-axis stator currents, A.
i_a, i_b, i_c	a-axis, b-axis and c-axis stator currents, A.
$u_{s\alpha}$, $u_{s\beta}$	α-axis and β-axis stator voltages, V.
u_{sd}, u_{sq}	d-axis and q-axis stator voltages, V.
ω_f, ω_r,ω_s	Slip frequency, angular rotor speed, synchronous angular velocity, rad/s.
L_m, L_s, L_r	Mutual inductance, stator, rotor inductances, H.
$\square^*$	Reference quantity.
θ	Rotor position.
σ	$(=1-(L_m{}^2/L_sL_r))$ Total leakage coefficient.
R_s, R_r	Stator and rotor resistances, Ω.
T_r	$(=L_r/R_r)$ Rotor time constant.
U_{dc}	DC link voltage, V.
T_L	Rated torque, N·m.
x_d, x_q	Disturbance caused by parameter variations and other unmodeled dynamics uncertainties.
ε_d, ε_q	Unstructured uncertainties.
P_N	Rated power, kW.
U_N	Rated voltage, V.
I_N	Rated current, A.

Manuscript received June 20, 2020; revised September 19, 2020; accepted December 22, 2020. Date of publication December 31, 2020; date of current version March 5, 2021. This work was supported in part by China Postdoctoral Science Foundation under Grant 2020M683524, in part by the Nature Science Basic Research Plan in Shaanxi Province under Grant 2020JQ-631, in part by the State Key Laboratory of Electrical Insulation and Power Equipment under Grant EIPE20201, in part by the National Natural Science Foundation of China under Grant 51677150, in part by the Key Research and Development Project of ShaanXi Province under Grant 2019GY-060, in part by the Key Laboratory of Industrial Automation in ShaanXi Province under Grant SLGPT2019KF01-12, in part by Shaanxi Outstanding Youth Fund under Grant 2020JC-40, and in part by the Key Laboratory of Power Electronic Devices and High Efficiency Power Conversion in Xi'an under Grant 2019219814SYS013CG035. Recommended for publication by Associate Editor G. Escobar. *(Corresponding author: Zhonggang Yin.)*

Zhonggang Yin and Cong Bai are with the School of Electrical Engineering, Xi'an University of Technology, Xi'an 710048, China (e-mail: zhgyin@xaut.edu.cn; baicong123@xaut.edu.cn).

Na Du is with the Xi'an Research Institute of Huawei Technologies Co., Ltd., Xi'an 710075, China (e-mail: xautduna@163.com).

Chao Du is with the School of Electrical and Control Engineering, Shaanxi University of Science and Technology, Xi'an 710021, China (e-mail: duchaoworkhard@163.com).

Jing Liu is with the School of Electrical Engineering, Xi'an University of Technology, Xi'an 710048, China (e-mail: jingliu@xaut.edu.cn).

Color versions of one or more figures in this article are available at https://doi.org/10.1109/TPEL.2020.3048429.

Digital Object Identifier 10.1109/TPEL.2020.3048429

I. INTRODUCTION

INDUCTION motor (IM) has many advantages, such as simple structure, reliable operation, and low cost. IM has been accepted widely in various industrial fields, such as the chemical and textile industry owing to its superiority. However, the IM is a high order, nonlinear, multivariable, and strong coupling system [1]. Therefore, to improve the motor performance, various control technologies have been developed by relevant researchers, such as sliding mode control (SMC) [2], [3], model predictive control (MPC) [4], [5], repetitive control (RC) [6], H_∞ control [7], and internal model control (IMC) [8].

SMC is suitable for designing the controller of the nonlinear system owing to its insensitivity to external disturbance and simple implementation [9]–[12]. In [13], a novel reaching law of SMC instead of traditional PI controller was proposed. Simulation and experimental results indicate that not only the chattering is reduced by the proposed controller, but also the reaching rate is improved. In [14], SMC was designed based on the nonlinear reaching law to achieve better performance of the speed-control for each ac motor. Simulation results indicate that the performances both in the steady state and transient process are improved. However, SMC has not been used widely in the actual application, because of the chattering caused by the switching function. In addition, there will be a singular problem if the SMC parameters are not selected properly. MPC is used in the field of nonlinear control [15], MPC has the advantages of

fast current response and relatively easy implementation [16], [17], and it has gained widespread acceptance for the current controller capable of high dynamic responses. In [18], the predictive current control method discussed chooses the best possible switching state of the converter at fixed sampling intervals, based on an evaluation criterion and predictions of the system behavior. In [19], a finite control set model predictive current control scheme based on virtual voltage vectors was proposed for five-phase permanent magnet synchronous machines, which aimed to reduce the low-order harmonic components of stator currents. Simulation and hardware-in-loop experimental results have verified the validity and effectiveness of the proposed scheme. In [20], the study proposes an integrated solution for MMC by combining the predictive control with the classical energy balancing approach. The proposed approach generates an output current waveform with the lowest switching ripple as compared with the fast MPC method. Thereby, the size of the output filter to eliminate the switching ripple is significantly minimized. The current tracking capability of the proposed approach is marginally deteriorated compared with fast MPC. However, the proposed MPC method still requires a higher number of switching states compared with fast MPC. The precise control signal can be achieved by an accurate controlled plant in MPC [21], [22]. However, the motor parameters will change during the motor operation. In addition, MPC has a higher requirement for CPU because of a mass of calculations in MPC. This is also the main reason for MPC cannot be widely used as expected. RC is well known for its high performance in a feedback system that is subject to periodic exogenous inputs, and it is applied in the control field for many industrial applications [23]–[25]. In [26], finite-dimensional robust repetitive controller (FDRRC) starting from the conventional repetitive controller is proposed. The experimental results indicate that the periodic disturbance is eliminated effectively, and the tracking performance is improved. However, the further work is still needed to reduce the complexity of FDRRC. H_∞ control is a method of designing multivariable input and multivariable output robust control systems in the modern control theory, and it has the advantages of excellent regulation performance and robust stability [27]. In [28], to solve the problem that the surface permanent magnet synchronous motor (SPMSM) speed control system is sensitive to internal parameter disturbance and external load disturbance during operation, the H_∞ robust current controller is designed based on Hamilton-Jacobi inequality to ensure the robustness of current control under the nominal mathematical model of SPMSM. The experiments verify the effectiveness and usability of the proposed control strategy.

IMC has the advantages of less computational burden, and simple implementation [29]. In [30] and [31], a current controller is designed based on the IMC principle. Not only the tunable parameters are reduced, but also the system robustness is improved. In [32], a novel application of IMC for spiral trajectories tracking was proposed. The zero steady-state tracking error can be achieved based on the proposed IMC, when the amplitude of the reference sinusoid changes linearly with time. In [33], a modified IMC scheme for speed regulation is proposed on the basis of a two-port IMC method, which effectively reduces the sensitivity to control input saturation of the standard IMC and leads to good tracking and disturbance rejection performances. In addition, the IMC controller also contains harmonics of the reference frequency to reduce the experimental tracking error caused by the nonlinearities, such as piezo actuator hysteresis and cross coupling. However, there are two problems in the conventional IMC. First of all, IMC has only one adjustable parameter, but the tracking performance and anti-disturbance performance need to be separated. Second, the system robustness cannot be guaranteed by the unchanging filter time constant of IMC with the lump of time-varying disturbance, namely, the disturbance caused by the parameter variations, model mismatch, and step load change cannot be eliminated effectively by an internal model controller. Therefore, the method of disturbance observation is introduced into motor control, and the time-varying disturbance is compensated, such as extended state observer (ESO) and Luenberger disturbance observer (LDO). In [34], since such approaches introduce certain feedback gains for the state variable, observers are needed that calculate the estimation of the state variable on the basis of directly measurable quantities. The Luenberger observers solve this task via introducing a differential equation for the estimated state. In [35], the fractional part of the total delay is considered for further assessment in the RPCC. Based on the plant extended state-space model, a modified Luenberger prediction observer with complete state feedback is designed to achieve a deadbeat response and estimate the state vector at the next sampling time. However, these RPCC still suffer from steady-state current errors due to the disturbance caused by parameter mismatch and other unmodeled dynamics.

In this article, a novel internal model control method of IM based on a LDO is proposed. The LDO is constructed based on the system state equation. First, the error between the measured current and observed current is considered as the system feedback. Then, in order to make the feedback error close to zero quickly, an appropriate feedback gain is chosen by the observer poles assignment. The feedback gain ensures that the observed disturbance is approximate to the system state variables. Finally, the disturbance can be acquired, which is measured difficultly. To tune the proposed scheme properly, a stability analysis based on Jury criterion has been used to determine the selection of the observer gain. The contributions of the proposed controller are as follows. First, the internal model control has many advantages such as practicability, simple structure, fewer online adjustment parameters, and regulation compared with PI. However, the internal model control cannot eliminate the time-varying disturbance effectively by the constant filter time constant. Therefore, a LDO is simply chosen as the estimated disturbance function, which varies with different operating conditions. The internal model control with LDO based on IM drive achieves fast and small overshoot current response. Second, the internal model control with LDO overcomes the weakness of current fluctuation of the conventional internal model control. The experiment is implemented on the IM drives based on DSP TMS320F28335. The experimental results indicate that the system disturbance can be estimated in real-time by LDO, IMC-LDO has better start-up performance and stronger robustness in case of parameter variations and step load change, and the feasibility and effectiveness of the proposed method are verified.

II. IM Control Method Based on Internal Model Principle

A. Mathematical Model of the IM

The voltage equation of IM under the *d-q* rotating coordinate system is given as

$$\begin{bmatrix} u_{sd} \\ u_{sq} \\ u_{rd} \\ u_{rq} \end{bmatrix} = \begin{bmatrix} R_s + L_s D & -\omega_s L_s & L_m D & -\omega_s L_m \\ \omega_s L_s & R_s + L_s D & \omega_s L_m & L_m D \\ L_m p & -\omega_f L_m & R_r + L_r D & -\omega_f L_r \\ \omega_f L_m & L_m D & \omega_f L_r & R_r + L_r D \end{bmatrix} \times \begin{bmatrix} i_{sd} \\ i_{sq} \\ i_{rd} \\ i_{rq} \end{bmatrix} \tag{1}$$

where D is a differential operator. Considering the multiple rotor bars connected by short-circuit rings in a squirrel cage motor, u_{rd} and u_{rq} are set to zero. At the same time, set $\psi_{rq} = 0$, and (1) can be rewritten as

$$\begin{bmatrix} u_{sd} \\ u_{sq} \end{bmatrix} = \begin{bmatrix} R_s + \sigma L_s D & -\omega_s \sigma L_s & (L_m/L_r)D \\ \omega_s \sigma L_s & R_s + \sigma L_s D & (L_m/L_r)\omega_s \end{bmatrix} \begin{bmatrix} i_{sd} \\ i_{sq} \\ \psi_{rd} \end{bmatrix} \tag{2}$$

where ψ_{rd} is the direct component of rotor flux. After the magnetic field orientation, the rotor flux $\psi_{rq} = 0$, here

$$T_r D\psi_{rd} + \psi_{rd} = L_m i_{sd}. \tag{3}$$

It can be seen that $\psi_{rd} = L_m i_{sd}$ is constant in steady state, and ψ_{rd} varies with i_{sd} under dynamic operation. Hence, it is necessary to keep ψ_{rd} / L_m and rotor flux ψ_{rd} as constant in the process of the motor speed control, substituting $u_{sq}{}' = u_{sq}$-$\omega_s(L_m/L_r)\psi_{rd}$ into (2), and making the Laplace transform. Then, (2) is formed as [31]

$$\begin{bmatrix} u_{sd}(s) \\ u'_{sq}(s) \end{bmatrix} = \begin{bmatrix} R_s + \sigma s L_s & -\omega_s \sigma L_s \\ \omega_s \sigma L_s & R_s + \sigma s L_s \end{bmatrix} \begin{bmatrix} i_{sd}(s) \\ i_{sq}(s) \end{bmatrix}. \tag{4}$$

Equation (4) can be equivalent to

$$\boldsymbol{Y}(s) = \boldsymbol{G}(s)\boldsymbol{U}(s)$$

where $\boldsymbol{U}(s) = [\,u_{sd}(s)\ u'_{sq}(s)\,]^T$, $\boldsymbol{Y}(s) = [\,i_{sd}(s)\ i_{sq}(s)\,]^T$, $\boldsymbol{G}(s) = \begin{bmatrix} \sigma s L_s + R_s & -\omega_s \sigma L_s \\ \omega_s \sigma L_s & \sigma s L_s + R_s \end{bmatrix}^{-1}$.

B. Design of the IMC Current Regulator

The block diagram of an IM control system based on IMC is demonstrated in Fig. 1, where ASR indicates speed regulator. For the field-oriented control of IM, three control loops including the quadrature axis (*q*-axis) current-loop, the direct axis (*d*-axis) current-loop, and the speed-loop are considered. The traditional PI controller is adopted in the speed-loop, and the speed controller output is taken as the expectation of the torque current. The stator three phase currents i_a, i_b, and i_c are detected by hall electric current sensor, the two phase current $i_{s\alpha}$ and $i_{s\beta}$ can be obtained after being transformed to α-β coordinate system, and the two phase current i_{sd} and i_{sq} can be obtained after being transformed to the *d-q* coordinate system. The internal model controller is used instead of the PI controller in the current-loop. Then, the errors between i_{sd}, i_{sq} and the given current ($i_{sd}{}^*$, $i_{sq}{}^*$) are taken as the inputs of IMC, respectively. The outputs of the internal model controller are $u_{sd}{}^*$, $u_{sq}{}^*$, and then $u_{s\alpha}{}^*$, $u_{s\beta}{}^*$ can be obtained after being transformed to the α-β coordinate system. Finally, SVPWM modules output PWM signals to supply for the inverter.

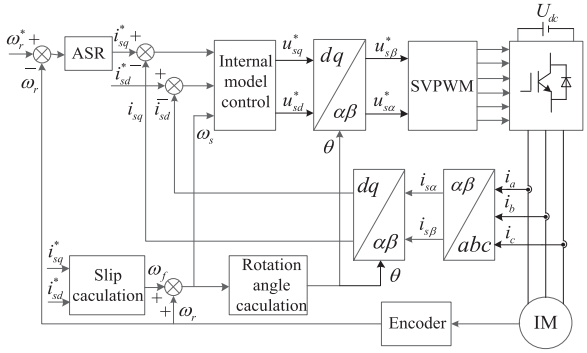

Fig. 1. Block diagram of IM control system based on the conventional IMC.

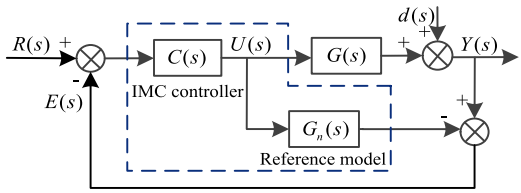

Fig. 2. Principle block diagram of IMC.

The fundamental idea of IMC is connecting an ideal internal model with the controlled object in parallel. The error between the reference model output and the controlled object output is used as the terminal input of the internal model controller. Furthermore, a low-pass filter is introduced to make the controller realizable.

Fig. 2 shows the structure of IMC, where *C*(*s*) is the internal model controller, *G*(*s*) is the controlled object, $G_n(s)$ is the reference model, *E*(*s*) is the feedback error signal, *R*(*s*) is the input of the controlled plant, *Y*(*s*) is the output of the controlled object, and *d*(*s*) is the external disturbance. The expression of the relation between the input and output according to Fig. 2 can be obtained as

$$Y(s) = \frac{C(s)G(s)}{1 + C(s)[G(s) - G_n(s)]}R(s) + \frac{1 - C(s)G_n(s)}{1 + C(s)[G(s) - G_n(s)]}d(s). \tag{5}$$

When the model is matching (ignoring the modeling error), namely, $G(s) = G_n(s)$. If the inverse of the controlled plant is used as the internal model controller, and the internal model controller can be expressed as

$$C(s) = {G_n}^{-1}(s). \tag{6}$$

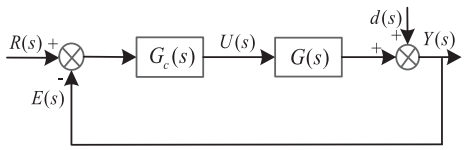

Fig. 3. Simplified schematic diagram of IMC.

Substituting (6) into (5), it can be obtained that $Y(s) = R(s)$, in other words, the system has strong robustness which is not affected by external disturbance d(s). Ideally, the internal model controller is implemented by the inverse model. However, the inverse model is difficult to achieve in practical application. Therefore, it needs to cascade a low-pass filter to solve this problem, and then the internal model controller is designed as

$$C(s) = f_1(s)G_{n-}^{-1}(s) \tag{7}$$

where $G_{n-}^{-1}(s)$ is the reversible part of the controlled plant and $f_1(s)$ is a low-pass filter which is designed as $f_1(s) = \frac{1}{\lambda_1 s+1}$.

Fig. 3 shows a simplified schematic diagram of IMC, $G_c(s)$ is the equivalent feedback controller, and it is deduced as

$$\begin{aligned} G_c(s) &= \frac{C(s)}{1 - C(s)G_n(s)} \\ &= \frac{1}{\lambda_1}\begin{bmatrix} \sigma L_s + R_s/s & -\omega_s \sigma L_s/s \\ \omega_s \sigma L_s/s & \sigma L_s + R_s/s \end{bmatrix}. \end{aligned} \tag{8}$$

C. Analysis of Stability and Robustness

When the model is mismatch, namely, $G(s) \neq G_n(s)$, the multiplicative uncertainty bound $\bar{l}_m(j\omega)$ is used to describe the model uncertainty, and $\eta(j\omega)$ is the complementary sensitivity function. For the unit negative feedback control system such as Fig. 3, the necessary and sufficient condition for the closed-loop system stability is

$$\left\| \eta(j\omega)\bar{l}_m(j\omega) \right\|_\infty < 1 \forall \omega \tag{9}$$

where $|l_m(j\omega)| = |\frac{G(j\omega)-G_n(j\omega)}{G_n(j\omega)}| \leq \overline{l_m}$, and $\eta(j\omega) = \frac{G_c(j\omega)G(j\omega)}{1+G_c(j\omega)G(j\omega)} = \frac{1}{\lambda_1 j\omega+1}$.

According to (8) and (9), the sufficient and necessary condition for the closed-loop system stability is given by

$$l_m \leq |\lambda_1(j\omega) + 1| \, \forall \omega. \tag{10}$$

Equation (10) shows that the robustness of the internal model control system can be guaranteed by adjusting the filter parameters. The bigger the λ_1 is, the bigger the toleration of the model uncertainty is. But in practical application, the system uncertainty is time-varying, and thus the system robustness cannot be guaranteed by the traditional internal model control.

According to [36], considering factors such as system robustness and interference suppression capabilities, the filter time constant λ_1 can be selected as ten times the sampling period. The current loop sampling time of the IM control system used in this article is 0.5 ms, so the filter time constant $\lambda_1 = 0.005$, the bandwidth of the current loop is $\alpha = 2\pi/\lambda_1 = 1256$ rad/s.

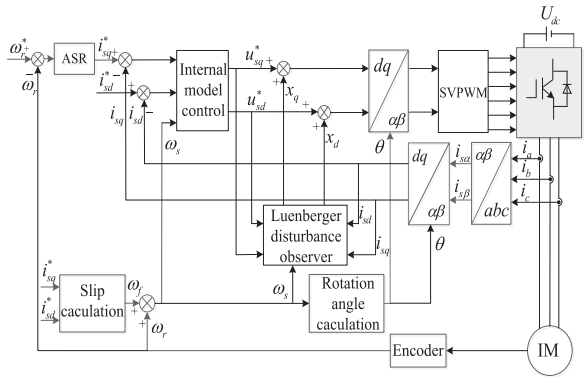

Fig. 4. Block diagram of IM control system based on IMC-LDO.

According to the bandwidth of the current loop and the closed-loop transfer function of IMC, the filter parameter λ_1 can be obtained.

IV. Internal Model Control Strategy for IMs Based on LDO

It should be noted from (10) that the system robustness cannot be guaranteed by the traditional IMC. First of all, IMC has only one adjustable parameter, but the tracking performance and anti-disturbance performance need to be separated. Second, the system robustness cannot be guaranteed by the unchanging filter time constant of IMC with the lump of time-varying disturbance. Therefore, an LDO is introduced to estimate the disturbance in real-time. Subsequently, it will be embedded in the current-loop.

Fig. 4 shows a block diagram of IM control system based on IMC-LDO, while LDO is embedded in the current-loop, and LDO is constructed based on the system state equation. First, the error between the measured current and the observed current is considered as the system feedback. Then, to enable the feedback error close to zero quickly, an appropriate feedback gain is chosen by the observer poles assignment. The feedback gain ensures the observed disturbance is approximate to the system state variables. Finally, the disturbance which is measured difficultly can be acquired.

A. Design of the LDO

The disturbance caused by parameter variations and unstructured uncertainties is considered in an IM system. Based on this system, LDO is designed to estimate the uncertainties of x_d and x_q offsets, which realizes the current-loop compensation. Set $L = \sigma L_s$, (11) can be obtained from (4)

$$\begin{bmatrix} u_{sd} \\ u_{sq} \end{bmatrix} = \begin{bmatrix} R_s i_{sd} - \omega_s L i_{sq} \\ R_s i_{sq} + \omega_s L i_{sd} \end{bmatrix} + L \begin{bmatrix} \frac{di_{sd}}{dt} \\ \frac{di_{sq}}{dt} \end{bmatrix} \tag{11}$$

Take into account the parameter variations and the unstructured uncertainties, the current-loop model is expressed as

$$\begin{cases} u_{sd} = -(L + \Delta L)\omega_s i_{sq} + (L + \Delta L)\frac{di_{sd}}{dt} \\ \qquad\qquad +(R_s + \Delta R)i_{sd} + \varepsilon_d \\ u_{sq} = (L + \Delta L)\omega_s i_{sd} + (L + \Delta L)\frac{di_{sq}}{dt} \\ \qquad\qquad +(R_s + \Delta R)i_{sq} + \varepsilon_q \end{cases} \tag{12}$$

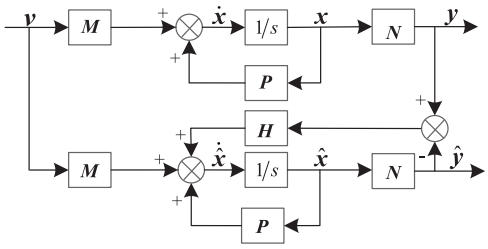

Fig. 5. Block diagram of LDO.

where ΔL and ΔR are the parametric uncertainties that can be considered as unknown slow variant signals. The total uncertainties are defined as

$$\begin{cases} x_d = -\Delta L\omega_s i_{sq} + \Delta L\frac{di_{sd}}{dt} + \Delta R i_{sd} + \varepsilon_d \\ x_q = \omega_s \Delta L i_{sd} + \Delta L\frac{di_{sq}}{dt} + \Delta R i_{sq} + \varepsilon_q. \end{cases} \tag{13}$$

Organizing (13), i_{sd}, i_{sq}, x_d, and x_q are chosen as state variables, then the state equation can be acquired

$$\dot{\boldsymbol{x}} = \boldsymbol{P}\boldsymbol{x} + \boldsymbol{M}\boldsymbol{v} \tag{14}$$

$$\boldsymbol{y} = \boldsymbol{N}\boldsymbol{x} \tag{15}$$

where $\boldsymbol{x} = [\,i_{sd}\ i_{sq}\ x_d\ x_q\,]^T$, $\boldsymbol{v} = [\,u_{sd}\ u_{sq}\,0\ 0\,]^T$,

$$\boldsymbol{P} = \begin{bmatrix} -\frac{R_s}{L} & \omega_s & \frac{1}{L} & 0 \\ -\omega_s & -\frac{R_s}{L} & 0 & \frac{1}{L} \\ 0 & 0 & 0 & 0 \\ 0 & 0 & 0 & 0 \end{bmatrix}, \quad \boldsymbol{M} = \begin{bmatrix} -\frac{1}{L} & 0 & 0\,0 \\ 0 & -\frac{1}{L} & 0\,0 \\ 0 & 0 & 0\,0 \\ 0 & 0 & 0\,0 \end{bmatrix},$$

$$\mathbf{N} = \begin{bmatrix} 1\,0\,0\,0 \\ 0\,1\,0\,0 \\ 1\,0\,0\,0 \\ 0\,1\,0\,0 \end{bmatrix}.$$

LDO is built by (14) and (15)

$$\dot{\hat{\boldsymbol{x}}} = \boldsymbol{P}\hat{\boldsymbol{x}} + \boldsymbol{M}\boldsymbol{v} + \boldsymbol{H}(\boldsymbol{y} - \hat{\boldsymbol{y}}) \tag{16}$$

$$\hat{\boldsymbol{y}} = \boldsymbol{N}\hat{\boldsymbol{x}} \tag{17}$$

where $\hat{\boldsymbol{x}} = [\,\hat{i}_{sd}\ \hat{i}_{sq}\ \hat{x}_d\ \hat{x}_q\,]^T$, $\hat{\boldsymbol{y}} = [\,\hat{i}_{sd}\ \hat{i}_{sq}\ \hat{i}_{sd}\ \hat{i}_{sq}\,]^T$, $\boldsymbol{H} = \begin{bmatrix} k_1 & 0 & 0 & 0 \\ 0 & k_1 & 0 & 0 \\ 0 & 0 & k_2 & 0 \\ 0 & 0 & 0 & k_2 \end{bmatrix}$.

Fig. 5 shows the structure of LDO, where $\hat{\boldsymbol{x}}$ is the estimated state variable, $\hat{\boldsymbol{y}}$ is the estimated output, and $\boldsymbol{H}$ is the feedback gain matrix of the observer.

The discrete LDO is given as

$$\begin{bmatrix} \hat{i}_{sd}(k+1) \\ \hat{i}_{sq}(k+1) \\ \hat{x}_d(k+1) \\ \hat{x}_q(k+1) \end{bmatrix} = \boldsymbol{A}\begin{bmatrix} \hat{i}_{sd}(k) \\ \hat{i}_{sq}(k) \\ \hat{x}_d(k) \\ \hat{x}_q(k) \end{bmatrix} + \frac{T_s}{L}\boldsymbol{u}(k) + \begin{bmatrix} k_1(i_{sd}(k) - \hat{i}_{sd}(k)) \\ k_1(i_{sq}(k) - \hat{i}_{sq}(k)) \\ k_2(i_{sd}(k) - \hat{i}_{sd}(k)) \\ k_2(i_{sq}(k) - \hat{i}_{sq}(k)) \end{bmatrix} \tag{18}$$

where $\boldsymbol{A} = \begin{bmatrix} 1 - \frac{T_s R_s}{L} & T_s\omega_s(k) & \frac{T_s}{L} & 0 \\ T_s\omega_s(k) & 1 - \frac{T_s R_s}{L} & 0 & \frac{T_s}{L} \\ 0 & 0 & 1 & 0 \\ 0 & 0 & 0 & 1 \end{bmatrix}$, $\boldsymbol{u}(k) = [\,u_{sd}(k)\ u_{sq}(k)\ 0\ 0\,]^T$.

B. Stability Analysis of the LDO

The state equation of LDO can be obtained from (18)

$$\begin{bmatrix} \hat{i}_{sd}(k+1) \\ \hat{i}_{sq}(k+1) \\ \hat{x}_d(k+1) \\ \hat{x}_q(k+1) \end{bmatrix} = (\boldsymbol{A} - \boldsymbol{H}\boldsymbol{N})\begin{bmatrix} \hat{i}_{sd}(k) \\ \hat{i}_{sq}(k) \\ \hat{x}_d(k) \\ \hat{x}_q(k) \end{bmatrix} + \frac{T_s}{L}\boldsymbol{u}(k) + \begin{bmatrix} k_1 i_{sd}(k) \\ k_1 i_{sq}(k) \\ k_2 i_{sd}(k) \\ k_2 i_{sq}(k) \end{bmatrix}. \tag{19}$$

Set $\boldsymbol{B} = (\boldsymbol{A} - \boldsymbol{H}\boldsymbol{N})$, the dynamic response of the discrete LDO hinges on the eigenvalues of the state equation coefficient matrix $\boldsymbol{B}$. When all eigenvalues distribute within the unit circle of the Z domain, the discrete LDO is stable.

The PWM interrupt frequency is 8 kHz in the experiment, and the small cross-coupling term $\omega_s(k)T_s$ can be ignored in the case ($\omega_s T_s < 0.00625$ for $\omega_s < 50$ Hz). Based on this, the characteristic equation of the disturbance observer is derived as (20) shown at the bottom of the next page, where $a_0 = k_2 b_2 T_s(k_2 b_2 T_s - b_1 T_s - k_1)$, $a_1 = k_2 b_2 T_s(b_1 T_s - k_1 - 1)$, $a_2 = k_2 b_2 T_s$, $b_1 = \frac{R_s}{L}$, $b_2 = \frac{1}{L}$.

The discrete LDO stability is analyzed by applying Jury criterion [37]. For (20), the necessary and sufficient conditions for the observer stability are

$$\begin{cases} \Delta(1) = a_2 + a_1 + a_0 > 0 \\ (-1)^2\Delta(-1) = a_2 - a_1 + a_0 > 0 \\ |a_0| < a_2. \end{cases} \tag{21}$$

After substituting a_0, a_1, a_2 into (21), we get

$$\begin{cases} k_2 b_2 T_s - b_1 T_s - 1 < k_1 < \frac{k_2 b_2 T_s}{2} \\ k_2 > 0. \end{cases} \tag{22}$$

Therefore, the selection of k_1, k_2 should satisfy formula (22) to guarantee the proposed observer stability.

C. State Errors Analysis of the LDO

Since the feedback is realized instead of x by $\hat{x}$. For the state estimation error$\boldsymbol{e}(t) = \boldsymbol{x}(t) - \hat{\boldsymbol{x}}(t)$. The time evolution of the state estimation error is given by

$$\boldsymbol{e}(t+1) = \boldsymbol{B}_{obs}(t)\boldsymbol{e}(t) \tag{23}$$

where $\boldsymbol{B}_{\rm obs}(t) = \boldsymbol{P} - \boldsymbol{H}\boldsymbol{N}$.

The following theorem proposes sufficient conditions ensuring the convergence of the estimation error.

Theorem 1: The state estimation error converges toward zero if there exists a symmetric, positive definite matrix $\boldsymbol{Q} \in \boldsymbol{R}^{n\times n}$and a matrix $\boldsymbol{S} \in \boldsymbol{R}^{n\times n}$solution of the constrained linear matrix

inequalities (LMI) problem:

$$\begin{bmatrix} (1-2\alpha)Q & P^TQ - N^TS^T \\ QP - SN^T & Q \end{bmatrix} > 0 \tag{24}$$

where the given decay rate is selected as $0 < \alpha < 0.5$.

Proof: This theorem is obtained by considering a quadratic Lyapunov function

$$V(e(t)) = e^T(t)Qe(t), Q > 0, Q = Q^T. \tag{25}$$

The convergence of the estimation error is guaranteed by [38]:

$$\exists Q = Q^T > 0, \alpha > 0 : \Delta V(e(t)) + 2\alpha V(e(t)) < 0 \tag{26}$$

where $\Delta V(e(t)) = V(e(t+1)) - V(e(t))$ and where α is the decay rate to ensure the convergence velocity. By using (25), the inequality becomes

$$e^T(t+1)Qe(t+1) - (1-2\alpha)V(e(t)) < 0 \tag{27}$$

which can be rewritten as follows considering (23)

$$e^T(t)\left\{B_{\text{obs}}^T(t)QB_{\text{obs}}(t) - (1-2\alpha)Q\right\}e(t) < 0. \tag{28}$$

Finally, the LMIs in theorem (1) are obtained using the well-known Schur complement [38]. Let us notice that adequate eigenvalues placement of the observer can be obtained by an appropriate choice of the decay rate α in theorem 1. For example, the convergence of the estimation error in (24) is obtained by considering $\alpha = 0.1$.

V. Experimental Verification

In order to validate the feasibility of the proposed method in this article, a contrast experiment is carried out by using a 1.1-kW IM. A 32-bits floating point digital signal processor TMS320F28335 is employed to accomplish the developed control algorithm. The IM parameters are listed in Table I. The experimental platform is shown in Fig. 6, which consists of three parts: the servo inverter, the loading system, and the control circuit. The filter parameter value in the internal model controller is selected as $\lambda_1 = 0.25$. The Lunberger disturbance observer gain is selected as $k_1 = 5, k_2 = 15$ here, which not only assures the stability but also balances the dynamic response and robustness of the proposed controller. Considering the motor power and the market condition, the switching frequency is selected as 8 kHz, the current sampling frequency is 2 kHz, and the speed sampling frequency is 0.5 kHz, respectively. The system hardware is composed of an IM inverter, an IM, an oscilloscope, and a loading system. The loading system is mainly composed of a servo inverter and a loading servo motor, and the IM is driven by the inverter. The stator current, stator voltage, and rotor speed are measured by a Hall effect current sensor, a Hall effect voltage sensor, and a photoelectric coder, respectively.

TABLE I
Motor Parameters

P_N	1.1 kW	R_s	5.27 Ω
U_N	380 V	R_r	5.07 Ω
I_N	2.7 A	L_m	0.421 H
f_N	50 Hz	L_s	0.423 H
T_L	7.5 N·m	L_r	0.479 H
J	0.02 kg·m^2	σL_s	0.053 H
n_N	1410 r/min	P	2

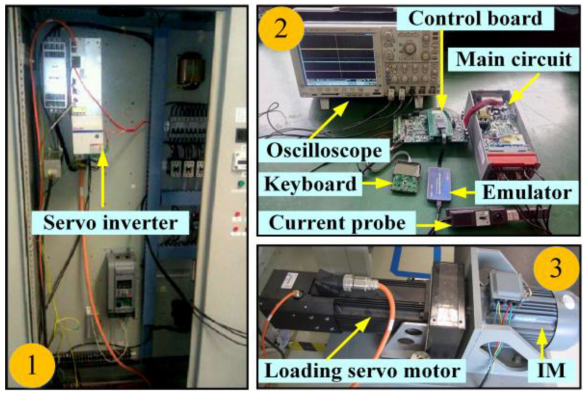

Fig. 6. Experimental platform.

The system software process consists of the over-voltage and over-current protection, initialization, main loop, current detection, PWM interrupt, etc. The period of the PWM interrupt is 125 μs, and the main functions include the IMC-LDO algorithm, coordinate transformation, dead time compensation, SVPWM generation, etc.

A. Experimental Verification During Full-Speed Range

Fig. 7 shows the given speed and rotor speed response based on IMC-LDO. As shown in Fig. 7, the motor runs at seven stages, including 30, 300, 900, 1500, 1200, 600, and 150 r/min,

$$\begin{aligned}\Delta(z) = |z\boldsymbol{I} - \boldsymbol{B}| &= \det\left(z\boldsymbol{I} - \begin{bmatrix} 1-\frac{T_sR_s}{L}-k_1 & T_s\omega_s(k) & \frac{T_s}{L} & 0 \\ T_s\omega_s(k) & 1-\frac{T_sR_s}{L}-k_1 & 0 & \frac{T_s}{L} \\ -k_2 & 0 & 1 & 0 \\ 0 & -k_2 & 0 & 1 \end{bmatrix}\right) \\ &= \det\begin{pmatrix} z-1+b_1T_s+k_1 & -T_s\omega_s(k) & -b_2T_s & 0 \\ -T_s\omega_s(k) & z-1+b_1T_s+k_1 & 0 & -b_2T_s \\ k_2 & 0 & z-1 & 0 \\ 0 & k_2 & 0 & z-1 \end{pmatrix} \\ &= (a_2z^2 + a_1z + a_0)^2 \end{aligned} \tag{20}$$

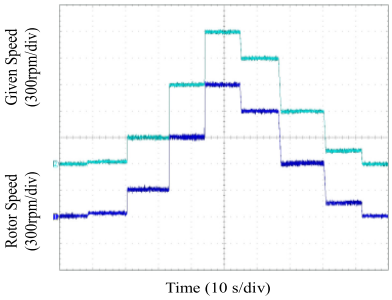

Fig. 7. Speed response in full speed range based on IMC-LDO.

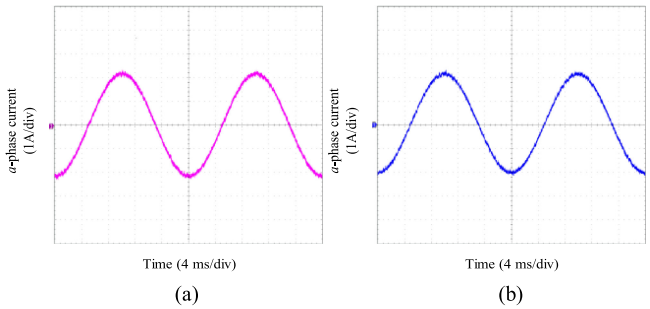

Fig. 8. Current contrast waveform. (a) Output waveform of stator current at 1500 r/min. (b) Standard sinusoidal current waveform.

respectively, which contains the full range of running speeds. This indicates that the proposed method has good tracking performance. Fig. 8(a) displays the output waveform of the stator current at 1500 r/min, and Fig. 8(b) shows the standard sinusoidal current waveform. The stator current is very close to the standard sinusoidal current. Therefore, it can be summarized that IMC-LDO can provide good steady and dynamic property in the full-speed range.

B. Verification of the Dynamic Performance

Fig. 9 shows the comparison of steady state and transient responses based on IMC and IMC-LDO with no load, and the rotor speed steps up to 1500 r/min from 150 r/min. Fig. 9(a) shows the current response based on IMC, Fig. 9(b) shows the current response based on IMC-LDO, Fig. 9(c) shows the rotor speed response based on IMC, and Fig. 9(d) shows the rotor speed response based on IMC-LDO. Comparing IMC and IMC-LDO with the same motor parameters, the speed overshoot decreases to 30 from 80 r/min, while the adjusting time of i_{sq} is shorter, and the overshoots of i_{sq} and rotor speed are smaller based on IMC-LDO. In conclusion, LDO can estimate the disturbance in real-time, and a better dynamic performance can be achieved based on IMC-LDO.

Because of the introduction of LDO in IMC, the dynamic performance is improved based on IMC-LDO. Fig. 10 shows the estimated disturbance x_d and x_q by LDO. In steady state, the disturbance is not large because of the small variations of the current and speed. However, in the dynamic stage, the disturbance is large because of the large variations of current and speed.

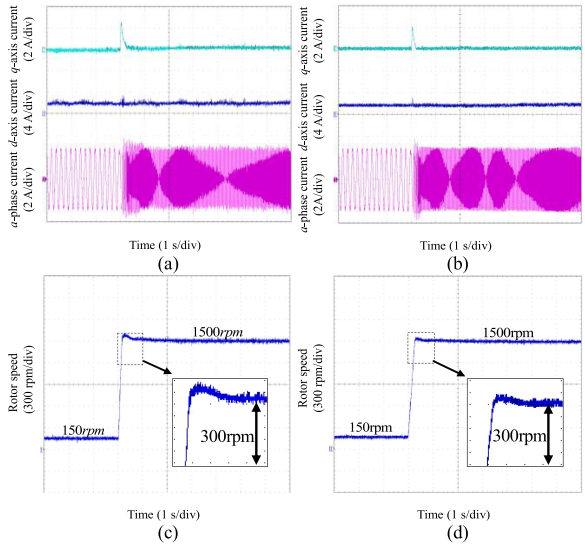

Fig. 9. Experimental comparison of the rotor speed and the current when the speed changes. (a) Current response of IMC. (b) Current response of IMC-LDO. (c) Speed response of IMC. (d) Speed response of IMC-LDO.

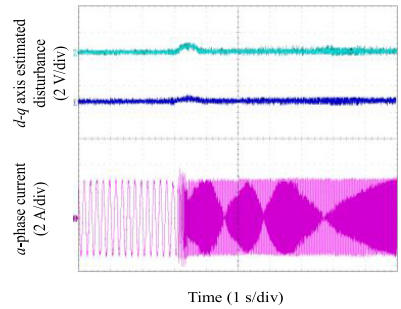

Fig. 10. Estimated disturbance of LDO when the speed changes.

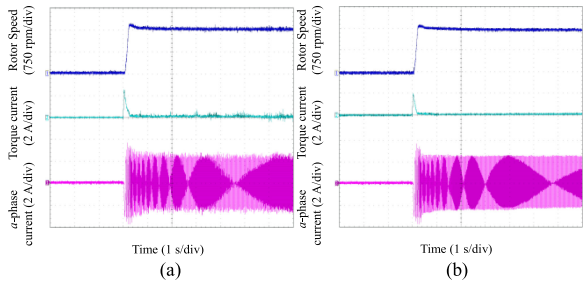

Fig. 11. Experimental comparison of the rotor speed and the current at 1500 r/min with 2 R_s. (a) IMC. (b) IMC-LDO.

C. Experimental Results With R_s Variation

Fig. 11 depicts the responses of the traditional IMC and the proposed IMC-LDO at 1500 r/min under R_s mismatch. Fig. 11(a) shows the rotor speed and the current based on IMC, and Fig. 11(b) shows the rotor speed and the current based on IMC-LDO. It can be seen that IMC results in a speed overshoot of 150 r/min while it is only 70 r/min in the case of IMC-LDO. In addition, the overshoot of i_{sq} is smaller in the transient process, and the fluctuation of i_{sq} is smaller under IMC-LDO with a mismatch R_s in the steady state.

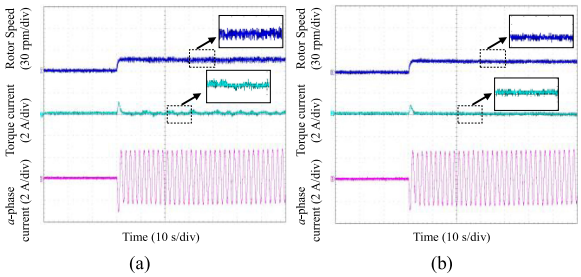

Fig. 12. Experimental comparison of the rotor speed and the current at 15 rpm with 2 R_s. (a) IMC. (b) IMC-LDO.

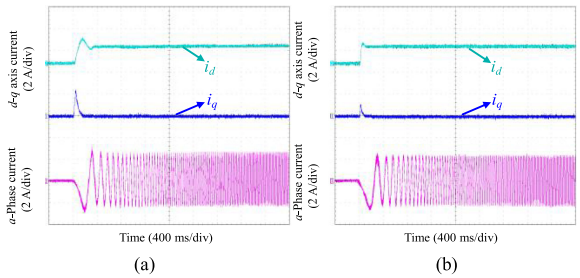

Fig. 13. Experimental comparison of the two controllers at 1500 r/min with 1.2 L_m. (a) IMC. (b) IMC-LDO.

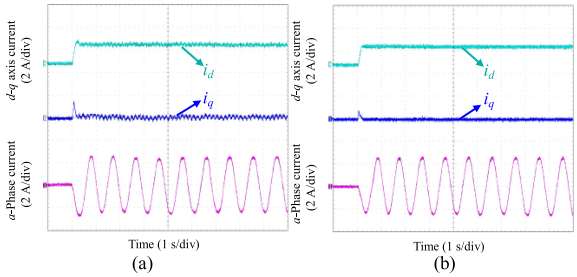

Fig. 14. Experimental comparison of the two controllers at 30 r/min with 1.2 L_m. (a) IMC. (b) IMC-LDO.

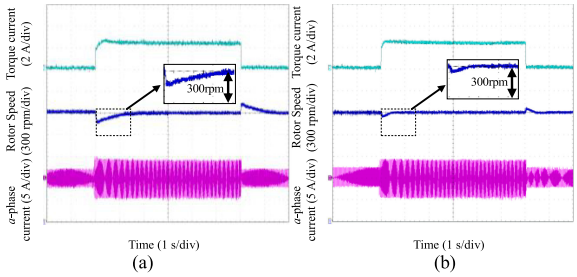

Fig. 15. Experimental comparison of the two controllers against a step rated load change at 1500 r/min. (a) IMC. (b) IMC-LDO.

Fig. 12 illustrates the responses of the traditional IMC and the proposed IMC-LDO at 15 r/min with 2 R_s. Fig. 12(a) shows the rotor speed and the current based on IMC, and Fig. 12(b) presents the rotor speed and the current based on IMC-LDO. It can be seen that the overshoot of i_{sq} is smaller in the transient process, and the fluctuation of i_{sq} and rotor speed is smaller under IMC-LDO with a mismatch R_s in the steady state. Fig. 12 indicates that IMC is more sensitive to the parameter variations. In other words, IMC-LDO has better robustness to the mismatched parameters.

D. Experimental Results With L_m Variation

Fig. 13 provides the responses of IMC and IMC-LDO at 1500 r/min under L_m mismatch when the rotor speed increases to 1500 r/min. Fig. 13(a) shows the responses of *d-q* axis current and *a*-phase current based on IMC, and Fig. 13(b) shows the responses of *d-q* axis current and *a*-phase current based on IMC-LDO. As the experimental results reveal, the current waveforms have a large overshoot and oscillation at start-up based on IMC, which are indeed the natural result of the poor relative stability of the control system under L_m variation. In contrast, the overshoot and oscillation are weakened effectively with the proposed scheme in Fig. 13(b). Generally, the proposed method can estimate the mutual inductance disturbance at start-up, and the overshoot and oscillation caused by L_m mismatch can be compensated by the estimated disturbance.

Fig. 14 provides the responses of the traditional IMC and the proposed IMC-IMDO under L_m mismatch when the rotor speed increases to 30 r/min. Fig. 14(a) shows the responses of *d-q* axis current and *a*-phase current based on IMC, and Fig. 14(b) shows the responses of *d-q* axis current and *a*-phase current based on IMC-LDO. As the experimental results reveal, the current waveforms have a large oscillation in Fig. 14(a), which are indeed the natural result of the poor relative stability for the control system under uncertainties. On contrary, the oscillation is weakened effectively, and an accurate current tracking performance is achieved in Fig. 14(b). Generally, the proposed method can estimate the mutual inductance disturbance at start-up, and the estimated disturbance can modify the oscillation caused by L_m mismatch.

E. Experimental Results With a Step Rated Load

Fig. 15 presents the responses of the traditional IMC and the proposed IMC-LDO with a step rated load at 1500 r/min. The rated load is added at $t = 2$ s and removed at $t = 8$ s. Fig. 15(a) presents the rotor speed and current based on IMC, and Fig. 15(b) presents the rotor speed based on IMC-LDO. From the experimental results, it can be seen that IMC results in a speed fluctuation of 120 r/min while it is only 60 r/min in the case of IMC-LDO. When the rated load is removed, the speed overshoot decreases to 60 from 120 r/min based on IMC-LDO, and the adjusting time of the rotor speed is smaller based on IMC-LDO. Generally, comparing IMC with IMC-LOD, IMC-LDO provides a clear improvement of the robustness and quickness at 1500 r/min.

Fig. 16 shows the estimated load disturbance x_d and x_q at 1500 r/min. It can be observed that LDO can estimate the disturbance caused by a step rated load change exactly and quickly with low chattering, and the system robustness is improved based on IMC-LDO.

Fig. 17 shows the responses of the traditional IMC and the proposed IMC-LDO with a step rated load change at 30 r/min. The rated load is added at $t = 4$ s and removed at $t = 16$ s.

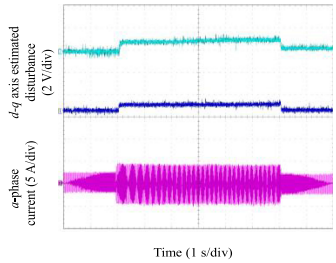

Fig. 16. Estimated disturbance of LDO with a step rated load change at 1500 r/min.

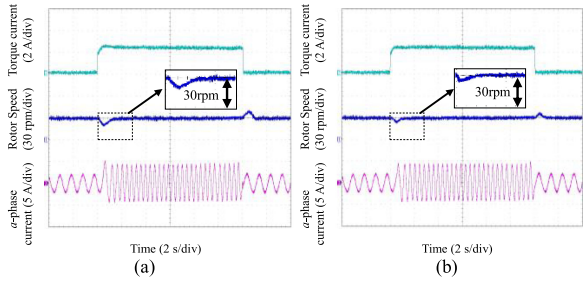

Fig. 17. Experimental comparison of the two controllers against step rated load change at 30 r/min. (a) IMC. (b) IMC-LDO.

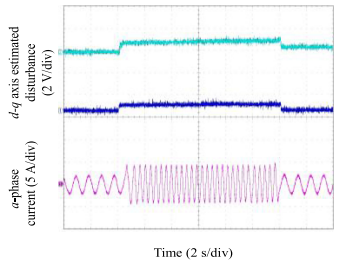

Fig. 18. Estimated disturbance of LDO with a step rated load change at 30 r/min.

Fig. 17(a) presents the rotor speed and the current based on IMC, and Fig. 17(b) presents the rotor speed based on IMC-LDO. From the experimental results, it can be seen that IMC results in a speed fluctuation of 12 r/min while it is only 6 r/min in the case of IMC-LDO. When the rated load is removed, the speed fluctuation decreases to 6 from 10 r/min based on IMC-LDO, and the adjusting time of the rotor speed is smaller based on IMC-LDO. In conclusion, IMC-LDO provides clear improvement of the robustness and quickness at 30 r/min.

Fig. 18 shows the estimated load disturbance x_d and x_q at 30 r/min. It can be found that LDO can estimate the disturbance caused by a step rated load change exactly and quickly with low chattering, and the system robustness is improved based on IMC-LDO.

V. Conclusion

Conventional IMC suffers from the problem that the robustness of the system cannot be guaranteed by IMC with time-varying disturbance when the motor operates. Considering the parameter variations and unstructured uncertainties in the IM system, a nonlinear current control algorithm for the IM systems using an internal model control strategy based on a LDO is proposed to optimize the current control performance of IM drives. The appropriate selection of the observer gain is given by applying Jury criterion, and the observer gain can balance the dynamic property and robustness of the proposed controller. In conclusion, IMC-LDO has better dynamic property and strong robustness in case of parameter variations and step rated load change. The effectiveness of the IMC-LDO scheme for the IM has been verified by the experimental results.

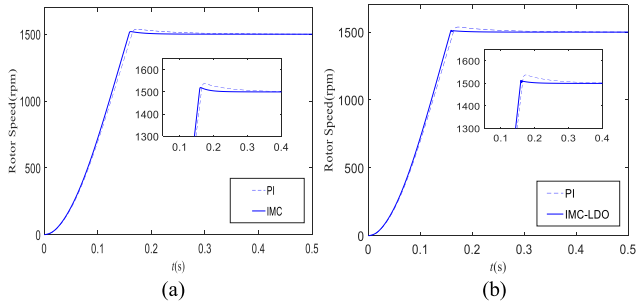

Fig. 19. Simulation comparison between PI, IMC, and IMC-LDO at start-up. (a) PI and IMC. (b) PI and IMC-LDO.

The Luenberger observer mentioned in [34] solves the problem that the system state is difficult to observe via introducing a differential equation for the estimated state. The Luenberger observer in [35] is a kind of Luenberger prediction observer, mainly to solve the fractional delays. Besides, the Luenberger observer proposed in this article is a kind of disturbance observer, which can effectively eliminate the time-varying disturbance and overcome the weakness of the current fluctuation of the conventional internal model control. The research contents to be carried out is analyzing whether the internal model control based on the Luenberger observer is suitable for the speed sensorless IM system.

Appendix

To verify the effectiveness of the proposed method in this article, multiple groups of contrast experiments are shown in Appendix. The parameters of the tested IM are shown in Table I.

A. Simulation Comparison of PI, IMC, and IMC-LDO

Fig. 19(a) shows the rotor speed waveforms of PI and IMC at start-up, and Fig. 19(b) shows the rotor speed waveforms of PI and IMC-LDO at start-up. The PI controller parameters have been tuned manually to be the best in the simulation. From the simulation results, it can be seen that the speed overshoot and adjusting time of PI are 35 r/min and 0.35 s, respectively, while they are 10 r/min and 0.2 s of the IMC-LDO. In conclusion, the proposed method shows a significant improvement compared with PI.

Fig. 20(a) shows the rotor speed waveforms of PI and IMC against step load change at 1500 r/min, and Fig. 20(b) shows the rotor speed waveforms of PI and IMC-LDO. The PI controller parameters have been tuned manually to be the best in the

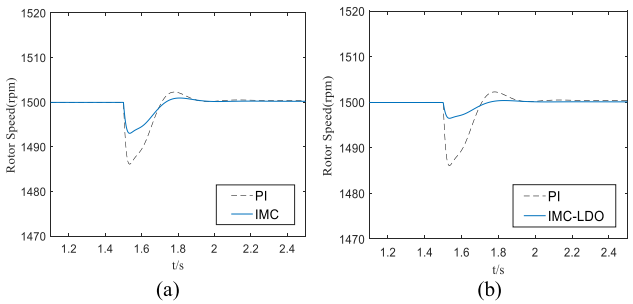

Fig. 20. Simulation comparison between PI, IMC, and IMC-LDO against step load change. (a) PI and IMC. (b) PI and IMC-LDO.

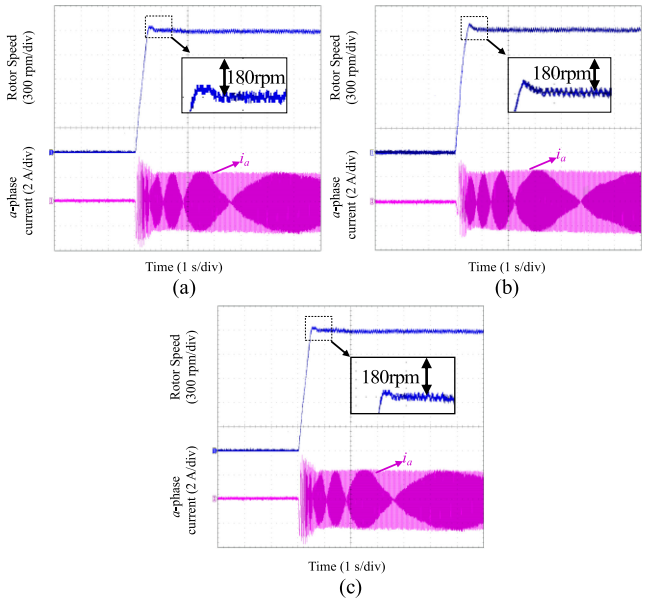

Fig. 21. Experimental comparison of the two controllers at 1500 r/min. (a) PI. (b) SMC. (c) IMC-LDO.

simulation. The rated load is added at $t = 1.5$ s, as can be seen from the figures, compared with PI, although the proposed IMC-LDO shows minor improvement in speed overshoot, it shows some improvement in adjusting time, which indicates that the dynamic performance of the system is effectively improved. Therefore, the proposed IMC-LDO is effective in improving the control performance of the IM control system.

B. Experimental Comparison of PI, SMC, and IMC-LDO

1) Experimental Results at Start-up: The comparison results between PI, SMC, and IMC-LDO are shown in Fig. 21. The rotor speed steps up to 1500 r/min with no load. The parameters of the PI and SMC controllers have been tuned manually to the best under the same parameters. Fig. 21(a)–(c) shows the experimental results based on PI, SMC, and IMC-LDO, respectively. Comparing the three controllers, the PI results in a speed overshoot of 60 r/min, the SMC results in a speed overshoot of 52 r/min while it is only 30 r/min in the case of IMC-LDO. The adjusting time of the rotor speed is the smallest based on IMC-LDO. Compared with PI and SMC, the speed fluctuation

TABLE II
COMPARISON RESULTS UNDER THE THREE METHODS

Performance Index \ Methods	PI	SMC	IMC-LDO
Speed overshoot/(rpm)	60	52	30
Adjusting time/(s)	0.65	0.6	0.5
IAE	379.5	303.9	301.5

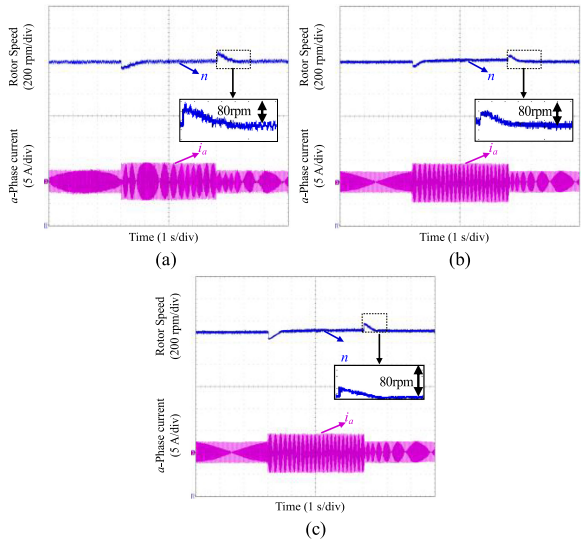

Fig. 22. Experimental comparison of the two controllers against step load change at 1500 r/min. (a) PI. (b) SMC. (c) IMC-LDO.

of IMC-LDO in steady state is the smallest. In conclusion, the adjusting time is the shortest, the speed overshoot is the smallest and the steady-state performance is the best based on IMC-LDO.

The integral absolute error (IAE) criterion is a standard performance index, which can be expressed as $\mathrm{IAE} = \int_0^T |r(t) - y(t)|dt$, where $r(t)$ and $y(t)$ are the reference input and measured variables, respectively and T is the time when the response tends to be stable. The comparison results of the three methods are shown in Table II. As can be seen in Table II, the overshoot, adjustment time, and IAE of the IMC-LDO control method proposed in this article are smaller than those of traditional PI and SMC control at 1500 r/min, which shows the superiority of the proposed IMC-LDO.

2) Experimental Results Against Step Load: Fig. 22 presents the responses of PI, SMC, and IMC-LDO against step load at 1500 r/min, and the rated load is added at $t = 3$ s and removed at $t = 7$ s. Fig. 22(a)–(c) presents the rotor speed and the a-phase current based on PI, SMC, and IMC-LDO, respectively. From the experimental results, it can be seen that PI and SMC result in a speed fluctuation of 80 and 60 r/min, respectively, while it is only 40 r/min in the case of IMC-LDO, which shows significant improvement in overshoot against step load. The adjusting time of PI, SMC, and IMC-LDO are 1, 0.6, and 0.4 s, respectively, which indicates that the proposed IMC-LDO has good dynamic performance and anti-load disturbance performance. The comparison results of the three methods are shown in Table III. As can be seen from Table III, the overshoot, adjustment time, and

TABLE III
COMPARISON RESULTS UNDER THE THREE METHODS

Performance Index \ Methods	PI	SMC	IMC-LDO
Speed overshoot/(rpm)	80	60	40
Adjusting time/(s)	1	0.6	0.4
IAE	40	18	8

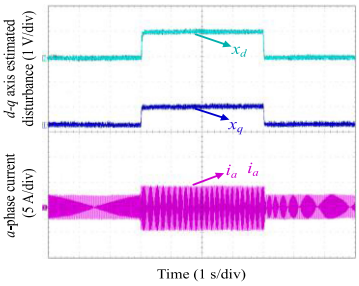

Fig. 23. Estimated disturbance of LDO against step load change at 1500 r/min.

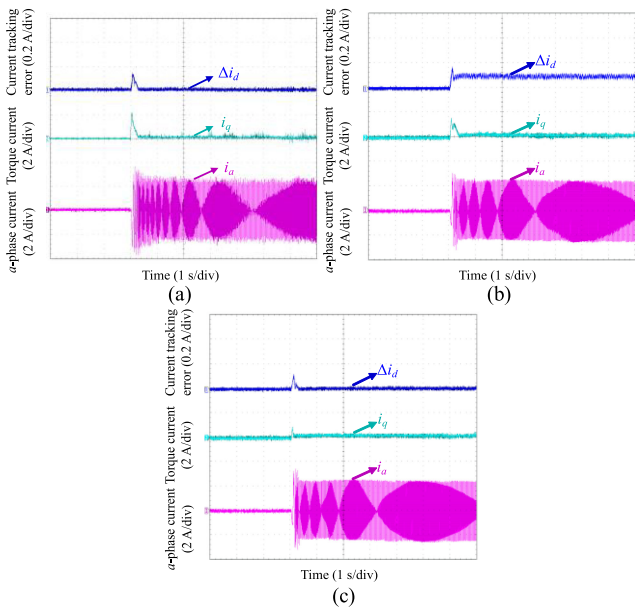

Fig. 24. Experimental comparison of the two controllers at 1500 r/min with 2 R_s. (a) PI. (b) SMC. (c) IMC-LDO.

IAE of the IMC-LDO control method proposed in this article are smaller than those of traditional PI and SMC control against step load change at 1500 r/min, which shows that the proposed IMC-LDO has better dynamic and steady-state performance.

Fig. 23 shows the estimated load disturbance x_d and x_q. It can be observed that LDO can estimate the disturbance caused by step load change exactly and quickly with low chattering, and the system robustness is improved based on IMC-LDO.

3) Experimental Results with R_s Variation: Fig. 24 provides the responses of PI, SMC, and IMC-LDO at 1500 r/min with 2 R_s. Fig. 24(a)–(c) presents the rotor speed and the a-phase current based on PI, SMC, and IMC-LDO, respectively. As the experimental results reveal, a steady-state error of 0.1 A results from the inaccuracy in the stator resistance based on SMC.

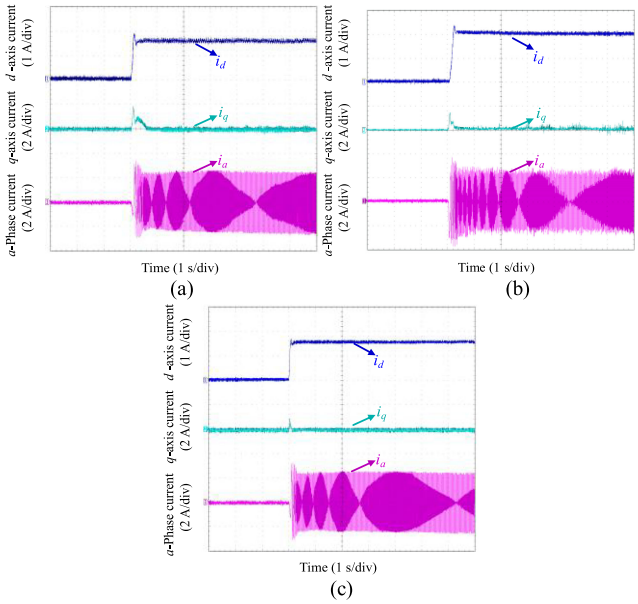

Fig. 25. Experimental comparison of the two controllers at 1500 r/min with 1.2 L_m. (a) PI. (b) SMC. (c) IMC-LDO.

However, the steady-state error is eliminated effectively based on IMC-LDO. In addition, the overshoot of i_q is the smallest in the transient process, and the fluctuation of Δi_d and i_q is the smallest under IMC-LDO with R_s mismatch in the steady state. It can be summarized that the proposed method can estimate the resistive disturbance, and the estimated disturbance converges to the steady value quickly.

4) Experimental Results With L_m Variation: Fig. 25 provides the responses of PI, SMC, and IMC-LDO at 1500 r/min under L_m mismatch when the rotor speed increases to 1500 r/min. Fig. 25(a)–(c) shows the responses of d-axis current and a-phase current based on PI, SMC, and IMC-LDO, respectively. As the experimental results reveal, the current waveforms have a large overshoot and oscillation at start-up based on PI and SMC, which are indeed the natural result of the poor relative stability of the control system under L_m variation. On the contrary, the overshoot and oscillation are weakened effectively based on IMC-LDO. Generally, IMC-LDO provides better parameter robustness against L_m variation. The current fluctuation of IMC-LDO is the smallest in steady state, the adjusting time is the shortest, and the speed overshoot is the smallest.

C. Experimental Comparison of IMC and IMC-LDO Based on Sensorless Vector Control

1) Experimental Results at Speed Reversal: The two control algorithms are compared under different operating conditions based on sensorless vector control (SVC). The responses during speed reversals are shown in Fig. 26. It can be seen that the motor decelerates quickly from 1500 to −1500 r/min. The dynamic responses of both methods are similar. In Fig. 26(b), the rotor speed remains stable and reliable based on IMC-LDO, the recovery time of the torque waveforms is smaller,

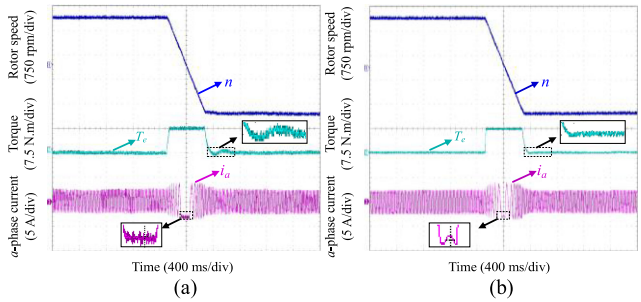

Fig. 26. Experimental comparison of the two controllers during speed reversal based on SVC at rated speed. (a) IMC. (b) IMC-LDO.

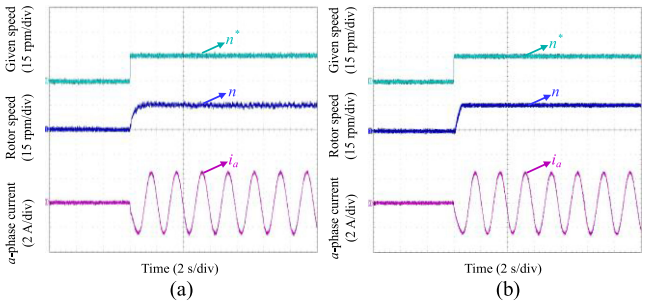

Fig. 27. Experimental comparison of the two controllers at 15 r/min. (a) IMC. (b) IMC-LDO.

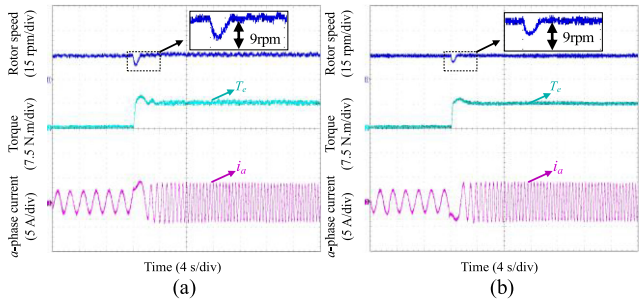

Fig. 28. Experimental comparison at 15 r/min with a step load. (a) IMC. (b) IMC-LDO.

and a smoother switching is achieved at the zero-crossing position. In general, IMC-LDO is evidently superior to IMC in terms of torque and current ripples.

2) Experimental Results at Low Speed: Fig. 27 shows the responses of the two controllers at low speed. Fig. 27(a) shows the given speed, estimated speed, and a-phase current based on IMC, and Fig. 27(b) presents the given speed, rotor speed, and a-phase current based on IMC-LDO. It can be seen that the rotor speed can track the given speed rapidly with no fluctuation based on IMC-LDO. On the contrary, the estimated speed starts slowly with ripple based on IMC. Furthermore, IMC-LDO based on SVC has better dynamic and steady-state performance at low speed.

3) Experimental Results With a Step Load at Low Speed: Fig. 28 shows the responses of the two methods at low speed, and the rated load is added at $t = 12$ s. Fig. 28(a) shows the rotor speed, torque, and a-phase current based on IMC, and Fig. 28(b)

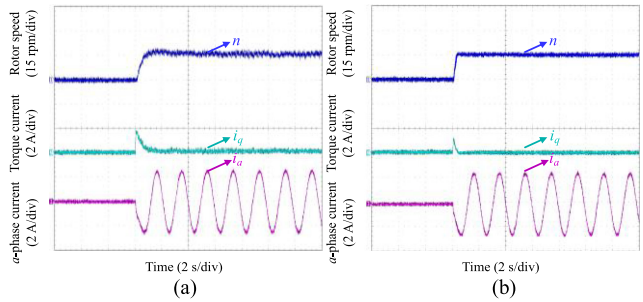

Fig. 29. Experimental comparison of the two controllers at 15 r/min with 2 R_s. (a) IMC. (b) IMC-LDO.

TABLE IV
MOTOR PARAMETERS

P_N	45 kW	R_s	2.52 Ω
U_N	380 V	R_r	5.75 Ω
I_N	85.4 A	L_m	0.362 H
f_N	50 Hz	L_s	0.362 H
T_L	286.5 N·m	σL_s	0.0159 H
n_N	1440 rpm	P	2

presents the rotor speed, torque, and a-phase current based on IMC-LDO. From the experimental results, it can be seen that IMC results in a speed fluctuation of 6 r/min while it is only 4 r/min in the case of IMC-LDO, and the adjusting time of the rotor speed is smaller based on IMC. It can be seen from the local enlargement of the steady state, the speed chattering is smaller based on IMC-LDO. Generally, IMC provides a better robustness and quickness performance at low speed against a step load.

4) Experimental Results With R_s Variation: To verify the performance of parameter variations, Fig. 29 shows the comparable results between the conventional IMC and the proposed IMC-LDO based on SVC. The resistance R_s is selected as the tested parameter. Fig. 29(a) shows the rotor speed and the current based on IMC, and Fig. 29(b) presents the rotor speed and the current based on IMC-LDO. It can be seen that the overshoot of i_q is smaller in the transient process, the adjusting time is shorter, and the rotor speed fluctuation is smaller under IMC-LDO in the steady state. Therefore, IMC-LDO has better robustness and quickness to the mismatched parameters at low speed.

D. Experimental Comparison of IMC and IMC-LDO Based on the High-Power Motor

To validate the feasibility of the proposed method based on the high-power motor, a contrast experiment is carried out by using a 45-kW IM. The IM parameters are listed in Table IV.

1) Experimental Results at Speed Reversal: The two control algorithms are compared under different operating conditions based on the high-power motor. The responses during speed reversals are shown in Fig. 30. It can be seen that the motor decelerates quickly from 1500 to −1500 r/min. The dynamic responses of both methods are similar. In Fig. 30(b), the rotor

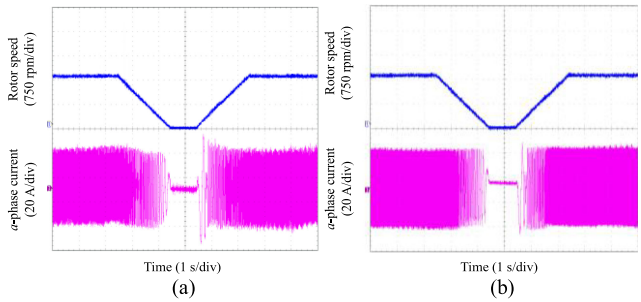

Fig. 30. Experimental comparison of the two controllers during speed reversal at rated speed. (a) IMC. (b) IMC-LDO.

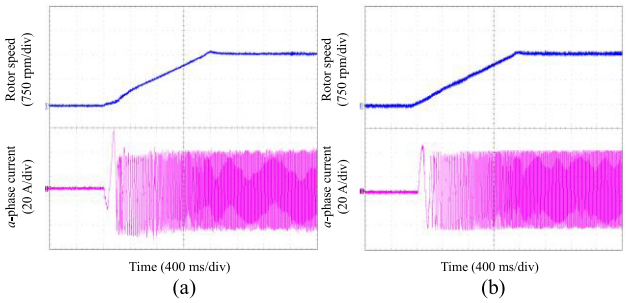

Fig. 31. Experimental comparison of the two controllers at 1500 r/min. (a) IMC. (b) IMC-LDO.

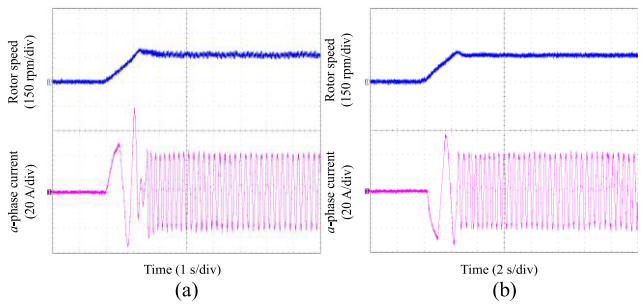

Fig. 32. Experimental comparison of the two controllers at 150 r/min with 2 R_s. (a) IMC. (b) IMC-LDO.

speed remains stable and reliable based on IMC-LDO, and a smoother switching is achieved at the zero-crossing position. In general, IMC-LDO is evidently superior to IMC in terms of the current ripples.

2) Verification of the Dynamic Performance: The comparison results between IMC and IMC-LDO are shown in Fig. 31. The rotor speed steps up to 1500 r/min with no load. Fig. 31(a) shows the experimental results based on IMC, and Fig. 31(b) shows the experimental results based on IMC-LDO. Comparing IMC and IMC-LDO, IMC controller results in a speed overshoot of 70 r/min while it is only 50 r/min in the case of IMC-LDO. Compared with IMC, the current fluctuation of IMC-LDO in steady state is smaller. In conclusion, the speed overshoot is smaller and the steady-state performance is better based on IMC-LDO.

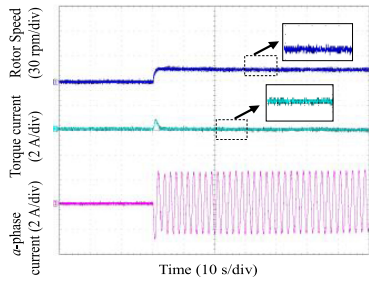

Fig. 33. Experimental result based on IMC-LDO with no load at 15 r/min.

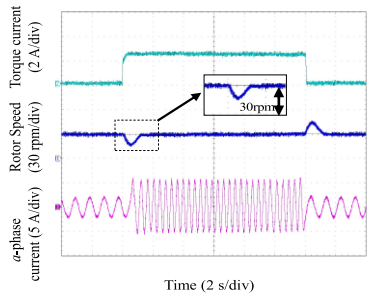

Fig. 34. Experimental results based on IMC-LDO with a step rated load from 0% to 150% rated torque at 30 r/min.

3) Experimental Results With R_s Variation: To verify the performance of parameter variations, Fig. 32 shows the comparable results between the conventional IMC and the proposed IMC-LDO. The resistance R_s is selected as the tested parameter. Fig. 32(a) shows the rotor speed and the current based on IMC, and Fig. 32(b) presents the rotor speed and the current based on IMC-LDO. It can be seen that the overshoot of the rotor speed is smaller in the transient process, the adjusting time is shorter, and the rotor speed fluctuation is smaller under IMC-LDO in the steady state. Therefore, IMC-LDO has better robustness and quickness to the mismatched parameters at low speed.

E. Experimental Verification During Low Speed and High Torque Condition

Fig. 33 shows the steady state and transient responses based on IMC-LDO with no load, and the rotor speed is 15 r/min. It can be seen that the overshoot of rotor speed and torque current is small in the transient process, and the fluctuation of rotor speed and torque current is also small under IMC-LDO. Fig. 33 indicates the feasibility and effectiveness of the proposed method under the condition of low speed.

In order to evaluate the effectiveness of the proposed method under high torque condition, a loading experiment is implemented at 30 r/min. Fig. 34 presents the experimental results based on IMC-LDO at 30 r/min when a step rated load with 150% rated torque is added. At the beginning, the motor is operating at 30 r/min with no load. Then a step rated load is added at $t =$ 4 s and removed at $t = 16$ s. It shows that the current waveform is not distorted and remains sine, the motor can operate stably and the control system based on IMC-LDO has good loading ability under high torque condition.

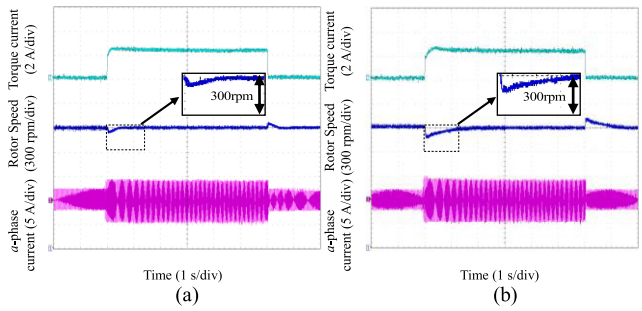

Fig. 35. Experimental comparison of the two observers against a step rated load change at 1500 r/min. (a) IMC-LDO. (b) IMC-ESO.

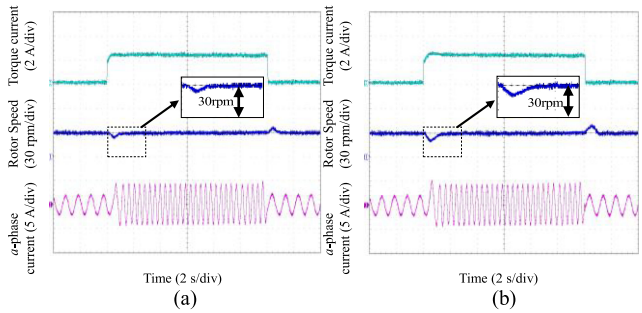

Fig. 36. Experimental comparison of the two observers against a step rated load change at 30 r/min. (a) IMC-LDO. (b) IMC-ESO.

TABLE V
COMPARISON RESULTS UNDER THE TWO METHODS

Methods / Performance Index	1500rpm		30rpm	
	IMC-LDO	IMC-ESO	IMC-LDO	IMC-ESO
Speed overshoot/(rpm)	60	110	9	12
Adjusting time/(s)	0.5	1	0.8	1
IAE	15	55	3.6	6

F. Experimental Comparison Between IMC-LDO and IMC-ESO

Fig. 35 presents an experimental comparison of the two observers against a step rated load change at 1500 r/min. Fig. 35(a) presents the rotor speed and current based on IMC-LDO, and Fig. 35(b) presents the rotor speed based on IMC-ESO. Fig. 36 presents an experimental comparison of the two observers against a step rated load change at 30 r/min. Fig. 36(a) presents the rotor speed and current based on IMC-LDO, and Fig. 36(b) presents the rotor speed based on IMC-ESO. From the experimental results, it can be seen that when the rated load is added and removed, the overshoot and adjustment time corresponding to the IMC-LDO is smaller than the overshoot and adjustment time corresponding to the IMC-ESO. The comparison results of the two methods are shown in Table V. It can be seen that the speed overshoot, adjustment time, and the IAE of the IMC-LDO are smaller than those of IMC-ESO against step load change at 1500 r/min and 30 r/min, which shows that the proposed LDO has better performance than the ESO.

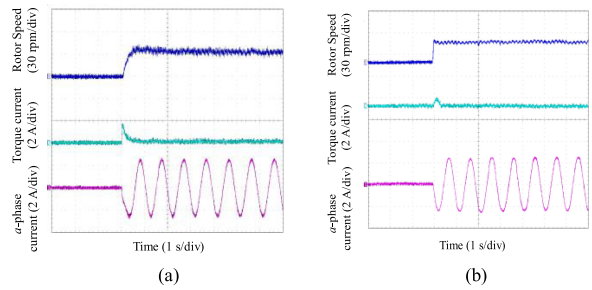

Fig. 37. Experimental comparison of the rotor speed and the current at 30 r/min with 3.5 R_s. (a) IMC. (b) IMC-LDO.

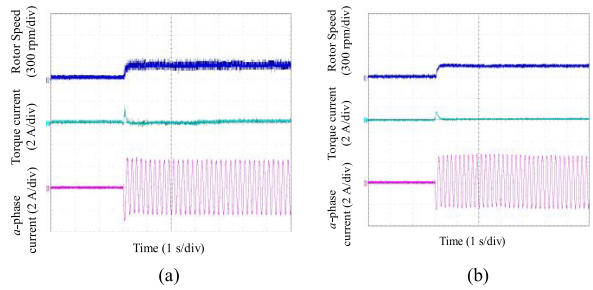

Fig. 38. Experimental comparison of the rotor speed and the current at 150 r/min with 3.5 R_s. (a) IMC. (b) IMC-LDO.

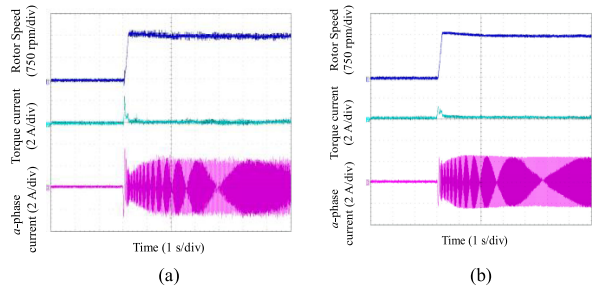

Fig. 39. Experimental comparison of the rotor speed and the current at 1500 r/min with 3.5 R_s. (a) IMC. (b) IMC-LDO.

G. Experimental Results With 3.5R_s Variation

Fig. 37 shows the responses of IMC and the proposed method at 30 r/min with 3.5 R_s. Fig. 37(a) and (b) shows the rotor speed and the current based on IMC and IMC-LDO, respectively. It can be seen that the adjusting time of the conventional IMC is longer than that of the proposed method. Moreover, the fluctuations of speed and current are smaller under the proposed method. Fig. 38 depicts the responses of the conventional IMC and the proposed method at 150 r/min with 3.5 R_s. It can be seen that IMC results in a relatively large rotor speed fluctuation while it is small in the case of IMC-LDO. Besides, the overshoot of the torque current is smaller in the transient process under the proposed IMC-LDO.

Fig. 39 illustrates the responses of the conventional IMC and the proposed IMC-LDO at 1500 r/min with 3.5 R_s. Fig. 39(a) and (b) shows the rotor speed and the current based on IMC and IMC-LDO, respectively. It can be seen that the overshoots and fluctuations of the torque current and speed are smaller

under the proposed method with 3.5 R_s. Figs. 37–39 indicate that the proposed method has better robustness when parameters mismatch.

H. Basic Principle of Luenberger Observer

The state observer can be established based on the state equation of the system. The Luenberger state observer makes a difference between the measurable and the estimated quantity of the system, then takes the error as the system feedback, next selects the appropriate gain of the feedback matrix through the pole assignment of the observer to make the feedback error close to zero. Therefore, the observed state quantity can quickly approach the system state quantity, and finally, the state quantity to be observed is obtained.

The design of the Luenberger state observer is as follows: the measurable state variable and the observed state variable are regarded as the state variables of the system, then the state equation of the controlled object is

$$\begin{cases} \dot{\boldsymbol{x}} = \boldsymbol{P}\boldsymbol{x} + \boldsymbol{M}\boldsymbol{v} \\ \boldsymbol{y} = \boldsymbol{N}\boldsymbol{x} \end{cases} \tag{29}$$

where $\boldsymbol{x}$ is the state variable of the system, $\boldsymbol{v}$ is the input of the system, and $\boldsymbol{y}$ is the output of the system.

Then, by using the feedback control principle, the output error $(\hat{\boldsymbol{y}} - \boldsymbol{y})$ of the system is introduced into the state in (29) of the controlled object through the feedback matrix $\boldsymbol{H}$, that is to say, the Luenberger state observer of the system is constructed as follows:

$$\begin{cases} \dot{\hat{\boldsymbol{x}}} = \boldsymbol{P}\hat{\boldsymbol{x}} + \boldsymbol{M}\boldsymbol{v} + \boldsymbol{H}(\boldsymbol{y} - \hat{\boldsymbol{y}}) \\ \hat{\boldsymbol{y}} = \boldsymbol{N}\hat{\boldsymbol{x}}. \end{cases} \tag{30}$$

The expression of system state estimation error is

$$\begin{aligned} \dot{\tilde{\boldsymbol{x}}} &= \dot{\boldsymbol{x}} - \dot{\hat{\boldsymbol{x}}} = (\boldsymbol{P}\boldsymbol{x} + \boldsymbol{M}\boldsymbol{v}) - (\boldsymbol{P}\hat{\boldsymbol{x}} + \boldsymbol{M}\boldsymbol{v} + \boldsymbol{H}\boldsymbol{y}) \\ &= \boldsymbol{P}(\boldsymbol{x} - \hat{\boldsymbol{x}}) - \boldsymbol{H}\boldsymbol{N}(\boldsymbol{x} - \hat{\boldsymbol{x}}) \\ &= (\boldsymbol{P} - \boldsymbol{H}\boldsymbol{N})(\boldsymbol{x} - \hat{\boldsymbol{x}}) \\ &= \tilde{\boldsymbol{P}}\tilde{\boldsymbol{x}}. \end{aligned} \tag{31}$$

The solution to this equation is

$$\tilde{\boldsymbol{x}}(t) = e^{\tilde{\boldsymbol{P}}t}\tilde{\boldsymbol{x}}(0). \tag{32}$$

It can be seen from (32) that the convergence rate of state estimation error depends on the eigenvalue of $\tilde{\boldsymbol{P}}$, that is, $\hat{\boldsymbol{x}}(t)$can converge to $\boldsymbol{x}(t)$ at any speed.

To solve the problem of how to configure the eigenvalues of $\boldsymbol{P} - \boldsymbol{H}\boldsymbol{N}$ arbitrarily, there are the following pole assignment theorems.

The state quantity of the system [**A**, **B**, **C**] can be estimated by the state observer in (31). The complete observability of the system [**A**, **B**, **C**] is a necessary and sufficient condition for the arbitrary assignment of its poles.

Proof: Based on the dual principle, if the system [**A**, **B**, **C**] is completely observable, then its dual system is completely controllable. Let the dual system be [**A**$*$, **B**$*$, **C**$*$], and then

$$\operatorname{rank}(s^*) = \operatorname{rank}[\,\boldsymbol{B}^*\ \boldsymbol{A}^*\boldsymbol{B}^*\ \boldsymbol{A}^{*2}\boldsymbol{B}^*\ \cdots\ \boldsymbol{A}^{*n-1}\boldsymbol{B}^*\,]. \tag{33}$$

Its poles can be configured arbitrarily by the state feedback matrix, since

$$\begin{aligned} &|s\boldsymbol{I} - (\boldsymbol{A}^* + \boldsymbol{B}^*\boldsymbol{K})| = \left|s\boldsymbol{I} - (\boldsymbol{A}^T + \boldsymbol{C}^T\boldsymbol{K})\right| \\ &\quad = \left|s\boldsymbol{I} - (\boldsymbol{A} + \boldsymbol{K}^T\boldsymbol{C})^T\right| = \left|s\boldsymbol{I} - (\boldsymbol{A} + \boldsymbol{K}^T\boldsymbol{C})\right|. \end{aligned} \tag{34}$$

So, make

$$\boldsymbol{K}^T = -\boldsymbol{H}. \tag{35}$$

Then, the following equation is obtained:

$$|s\boldsymbol{I} - (\boldsymbol{A}^* + \boldsymbol{B}^*\boldsymbol{K})| = |s\boldsymbol{I} - (\boldsymbol{P} - \boldsymbol{H}\boldsymbol{N})|. \tag{36}$$

The right side of the above-mentioned formula is the characteristic polynomial of the observer, and its poles can be arbitrarily allocated through the selection of $\boldsymbol{H}$.

REFERENCES

[1] B. Asghari and V. Dinavahi, "Experimental validation of a geometrical nonlinear permeance network based real-time induction machine model," *IEEE Trans. Ind. Electron.*, vol. 59, no. 11, pp. 4049–4062, Nov. 2012.

[2] S. C. Tan, Y. M. Lai, C. K. Tse, L. Martinez-Salamero, and C. K. Wu, "A fast-response sliding-mode controller for boost-type converters with a wide range of operating conditions," *IEEE Trans. Ind. Electron.*, vol. 54, no. 6, pp. 3276–3286, Dec. 2007.

[3] J. Liu, S. Laghrouche, and M. Wack, "Observer-based higher order sliding mode control of power factor in three-phase AC/DC converter for hybrid electric vehicle applications," *Int. J. Control*, vol. 87, no. 6, pp. 1117–1130, 2014.

[4] S. Vazquez *et al.*, "Model predictive control: A review of its applications in power electronics," *IEEE Ind. Electron. Mag.*, vol. 8, no. 1, pp. 16–31, Mar. 2014.

[5] G. L. Wang, Y. Wang, J. Xu, N. N. Zhao, and D. G. Xu, "Weight-transducerless rollback mitigation adopting enhanced MPC with extended state observer for direct-drive elevators," *IEEE Trans. Power Electron*, vol. 31, no. 6, pp. 4440–4451, Jun. 2016.

[6] R. Chuei, Z. W. Cao, and Z. H. Man, "Sliding mode based repetitive control for parameter uncertainty of a brushless DC servo motor," in *Proc. Int. Conf. Adv. Mechatronic Syst.*, 2016, pp. 62–67.

[7] J. Chen, H. Hou, and T. Yang, "Robust decentralized H∞ control for a multi-motor web-winding system," *IEEE Access*, vol. 7, pp. 41241–41249, 2019.

[8] R. Boukezzoula, S. Galichet, and L. Foulloy, "Nonlinear internal model control: Application of inverse model based fuzzy control," *IEEE Trans. Fuzzy Syst.*, vol. 11, no. 6, pp. 814–829, Dec. 2003.

[9] J. R. Dominguez, C. Mora-Soto, S. Ortega-Cisneros, J. J. Raygoza Panduro, and A. G. Loukianov, "Copper and core loss minimization for induction motors using high-order sliding-mode control," *IEEE Trans. Ind. Electron.*, vol. 59, no. 7, pp. 2877–2889, Jul. 2012.

[10] V. K. Singh and G. N. Pillai, "Non-singular fast terminal sliding mode control of general class of chaotic system," in *Proc. IEEE 6th IEEE Conf. Power Electron., Intell. Control Energy Syst.*, pp. 4–6, 2017.

[11] J.-X. Liu, S. Vazquez, L.-G. Wu, A. Marquez, H. J. Gao, and L. G. Franquelo, "Extended state observer-based sliding-mode control for three-phase power converters," *IEEE Trans. Ind. Electron.*, vol. 64, no. 1, pp. 22–31, Jan. 2017.

[12] A. Levant, "Higher-order sliding modes, differentiation and output feedback control," *Int. J. Control*, vol. 76, no. 9–10, pp. 924–941, 2003.

[13] X. G. Zhang, K. Zhao, and L. Sun, "A PMSM sliding mode control system based on a novel reaching law," in *Proc. Int. Conf. Elect. Mach. Syst.*, 2011, pp. 1–5.

[14] S. Y. Lin, Y. Z. Cai, and W. D. Zhang, "Electrical line-shafting control for motor speed synchronization using sliding mode controller and disturbance observer," *IET Control Theory Appl.*, vol. 11, no. 2, pp. 205–212, Jan. 2017.

[15] M. Siami, D. A. Khaburi, A. Abbaszadeh, and J. Rodríguez, "Robustness improvement of predictive current control using prediction error correction for permanent-magnet synchronous machines," *IEEE Trans. Ind. Electron.*, vol. 63, no. 6, pp. 3458–3466, Jun. 2016.

[16] J. Rodríguez *et al.*, "State of the art of finite control set model predictive control in power electronics," *IEEE Trans. Ind. Inf.*, vol. 9, no. 2, pp. 1003–1016, May 2013.
[17] P. Cortes, M. Kazmierkowski, R. Kennel, D. Quevedo, and J. Rodriguez, "Predictive control in power electronics and drives," *IEEE Trans. Ind. Electron.*, vol. 55, no. 12, pp. 4312–4324, Dec. 2008.
[18] J. Hong, D. Pan, and Z. J. Zong, "Comparison of the two current predictive control methods for a segment winding permanent magnet linear synchronous motor," *IEEE Trans. Plasma Sci.*, vol. 41, no. 5, pp. 1167–1173, May 2013.
[19] C. Xue, W. S. Song, and X. Y. Feng, "Finite control-set model predictive current control of five-phase permanent-magnet synchronous machine based on virtual voltage vectors," *IET Elect. Power Appl.*, vol. 11, no. 5, pp. 836–846, May 2017.
[20] A. Dekka, B. Wu, V. Yaramasu, and N. R. Zargari, "Integrated model predictive control with reduced switching frequency for modular multilevel converters," *IET Elect. Power Appl.*, vol. 11, no. 5, pp. 857–863, May 2017.
[21] J. J. Justo, F. Mwasilu, E. K. Kim, and H. H. Choi, "Fuzzy model predictive direct torque control of IPMSMS for electric vehicle applications," *IEEE Trans. Mechatronics*, vol. 11, no. 2, pp. 1–12, Feb. 2017.
[22] H. J. Wang, M. Yang, L. Niu, and D. G. Xu, "Improved deadbeat predictive current control strategy for permanent magnet motor drives," in *Proc. IEEE 6th Conf. Ind. Electron. Appl.*, 2011, pp. 1260–1264.
[23] S. F. Yang, P. Wang, Y. Tang, and L. Zhang, "Explicit phase lead filter design in repetitive control for voltage harmonic mitigation of VSI-based islanded microgrids," *IEEE Trans. Ind. Electron.*, vol. 64, no. 1, pp. 817–826, Jan. 2017.
[24] W. Lu, K. Zhou, D. Wang, and M. Cheng, "A generic digital nk $\pm$ m-order harmonic repetitive control scheme for PWM converters," *IEEE Trans. Ind. Electron.*, vol. 61, no. 3, pp. 1516–1527, Apr. 2013.
[25] B. Zhang, K. Zhou, and D. Wang, "Multirate repetitive control for PWM DC/AC converters," *IEEE Trans. Ind. Electron.*, vol. 61, no. 6, pp. 2883–2890, Jul. 2013.
[26] U. Mandal, A. Basu, S. Bose, A. Sengupta, and U. Saha, "Finite dimensional robust repetitive controller for tracking periodic reference input," in *Proc. IEEE Int. Conf. Elect., Comput. Commun. Technol.*, 2015, pp. 1–4.
[27] Y. Lee, S. Lee, and C. C. Chung, "LPV H∞ control with disturbance estimation for permanent magnet synchronous motors," *IEEE Trans. Ind. Electron.*, vol. 65, no. 1, pp. 488–497, Jan. 2018.
[28] W. Wang, H. Shen, L. Hou, and H. Gu, "H∞ robust control of permanent magnet synchronous motor based on PCHD," *IEEE Access*, vol. 7, pp. 49150–49156, 2019.
[29] C. Xia, Y. Yan, P. Song, and T. Shi, "Voltage disturbance rejection for matrix converter-based PMSM drive system using internal model control," *IEEE Trans. Ind. Electron.*, vol. 59, no. 1, pp. 361–372, Jun. 2015.
[30] C. K. Shiva and V. Mukherjee, "Comparative performance assessment of a novel quasi-oppositional harmony search algorithm and internal model control method for automatic generation control of power system," *IET Gener. Transm. Distrib.*, vol. 9, no. 11, pp. 1137–1150, Jun. 2015.
[31] Q. Zhu, Z.-G. Yin, Y.-Q. Zhang, J.-B. Niu, Y. Li, and Y.-R. Zhong, "Research on two-degree-of-freedom internal model control strategy for induction motor based on immune algorithm," *IEEE Trans. Ind. Electron.*, vol. 63, no. 3, pp. 1981–1992, Mar. 2016.
[32] A. Bazaei, Y.- K. Yong, and S. O. Reza Moheimani, "Combining spiral scanning and internal model control for sequential AFM imaging at video rate," *IEEE Trans. Mechatronics*, vol. 22, no. 1, pp. 371–380, Feb. 2017.
[33] S. Li and H. Gu, "Fuzzy adaptive internal model control schemes for PMSM speed-regulation system," *IEEE Trans. Ind. Inf.*, vol. 8, no. 4, pp. 767–779, Nov. 2012.
[34] K. Kósi, J. K. Tar, and T. Haidegger, "Application of Luenberger's observer in RFPT-based adaptive control—A case study," in *Proc. IEEE Int. Symp. Comput. Intell. Inf.*, 2013, pp. 365–369.
[35] J. R. Fischer, S. A. Gonzalez, M. A. Herran, M. G. Judewicz, and D. O. Carreca, "Calculation-delay tolerant predictive current controller for three phase inverters [J]," *IEEE Trans. Ind. Inf.*, vol. 10, no. 1, pp. 233–242, Feb. 2014.
[36] H. S. Lee *Robust Digital Tracking Controllers for High-speed/High-Accuracy Positioning Systems*. Berkeley, CA, USA: Univ. California, 1994.
[37] K. Ogata, *Discrete-Time Control Systems*. Englewood Cliffs, NJ, USA: Prentice Hall, 1987, ch. 4.
[38] S. Boyd, L. E.. Ghaoui, E. Feron, and V. Balakrishnan, *linear Matrix Inequalities in System and Control Theory*. Philadelphia, PA, USA: SIAM Stud. Appl. Math., vol. 15, 1994.

Zhonggang Yin (Member, IEEE) was born in Shandong, China, in 1982. He received the B.S., M.S., and Ph.D. degrees in electrical engineering from Xi'an University of Technology, Xi'an, China, in 2003, 2006, and 2009, respectively.

In 2009, he joined the Department of Electrical Engineering, Xi'an University of Technology, where he is currently a Professor. His research interests include high performance control of ac motor, and digital control of power converters.

Cong Bai was born in Shaanxi, China, in 1993. She received the B.S. degree in electrical engineering, in 2015 from Xi'an University of Technology, Xi'an, China, where she is currently working toward the Ph.D. degree in electric machines and electric apparatus.

Her main field of interests include high-performance control of linear motor.

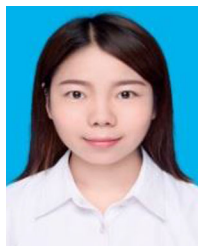

Na Du was born in Shaanxi, China, in 1993. She received the B.S. degree in electrical engineering from Xi'an University of Technology, Xi'an, China, in 2015.

She is currently working at the Xi'an Research Institute of Huawei Technologies Co., Ltd.

Chao Du was born in Shaanxi, China, in 1991. He received the B.S., M.S., and Ph.D. degrees in electronic engineering from Xi'an University of Technology, Xi'an, China, in 2013, 2016, and 2020, respectively.

In 2020, he joined the Department of Electrical and Control Engineering, Shaanxi University of Science and Technology, Xi'an, China. His research interests include high performance ac drive systems and its optimization of efficiency and parameters.

Jing Liu was born in Anhui, China, in 1982. She received the B.S., M.S., and Ph.D. degrees in electronic engineering from Xi'an University of Technology, Xi'an, China, in 2003, 2006, and 2009, respectively.

In 2009, she joined the Department of Electronic Engineering, Xi'an University of Technology, where she is currently an Associate Professor. Her research interests include the power semiconductor devices and their application to power electronic devices.